SUPPORTING INFORMATION FOR:

Highly performing LATP thin film electrolytes for all-solid-state microbattery applications

Valerie Siller,[a] Alex Morata,[,a] Marc Nuñez Eroles,[a] Raul Arenal,[b,c,d] Juan Carlos Gonzalez-Rosillo,[a] Juan Miguel López del Amo,[e] Albert Tarancón[*,a,f]*

[a] Catalonia Institute for Energy Research (IREC), Jardins de les Dones de Negre 1, Planta 2, 08930, Sant Adrià del Besòs, Barcelona, Spain.

[b] Instituto de Nanociencia y Materiales de Aragon (INMA), CSIC-Universidad de Zaragoza, Calle Pedro Cerbuna, 50009 Zaragoza, Spain

[c] Laboratorio de Microscopias Avanzadas (LMA), Universidad de Zaragoza, Calle Mariano Esquillor, 50018 Zaragoza, Spain

[d] Fundacion ARAID, 50018 Zaragoza, Spain

[e] Centre for Cooperative Research on Alternative Energies (CIC energiGUNE), Basque Research and Technology Alliance (BRTA), Alava Technology Park, Albert Einstein 48, 01510 Vitoria-Gasteiz, Spain.

[f] Catalan Institution for Research and Advanced Studies (ICREA), Passeig Lluís Companys 23, 08010, Barcelona, Spain

AUTHOR INFORMATION

Corresponding Author

*E-mail: atarancon@irec.cat

* E-mail: amorata@irec.cat

ORCID:

Valerie Siller: 0000-0001-5477-6304

Alex Morata : 0000-0002-3300-4636

Marc Nuñez Eroles : 0000-0002-6898-198X

Raul Arenal : 0000-0002-2071-9093

Juan Carlos Gonzalez-Rosillo : 0000-0001-6017-174X

Juan Miguel López del Amo : 0000-0002-2315-5414

Albert Tarancón : 0000-0002-1933-2406

Characterization

Target

The target revealed in X-ray diffractograms the phase of $LiTi_2(PO_4)_3$ (JCPDS 00-035-0754) with a slight peak shift towards higher diffraction angles due to the Al-dopant concentration of x = 0.56 measured by energy dispersive spectrometry (EDS). This structure has first been synthesized and studied by *Aono et al.*[1] and further analyzed in respect to its defect chemistry, ion transport mechanism and the effect of secondary phases with great detail in literature.[2,3] Additional phases in the sintered target were detected by XRD (see Fig. S1). Especially $AlPO_4$ appeared in higher amounts in the target, due to the elevated sintering temperatures causing a high volatility of Li_2O.[4,5] Raman spectra only revealed the $LiTi_2(PO_4)_3$ (LTP) phase (see Fig. S2), which may result from the high Raman activity of the solid electrolyte in comparison to potential

secondary phases, with especially $AlPO_4$ Raman spectra overlapping in the vibrational modes of LTP.[6]

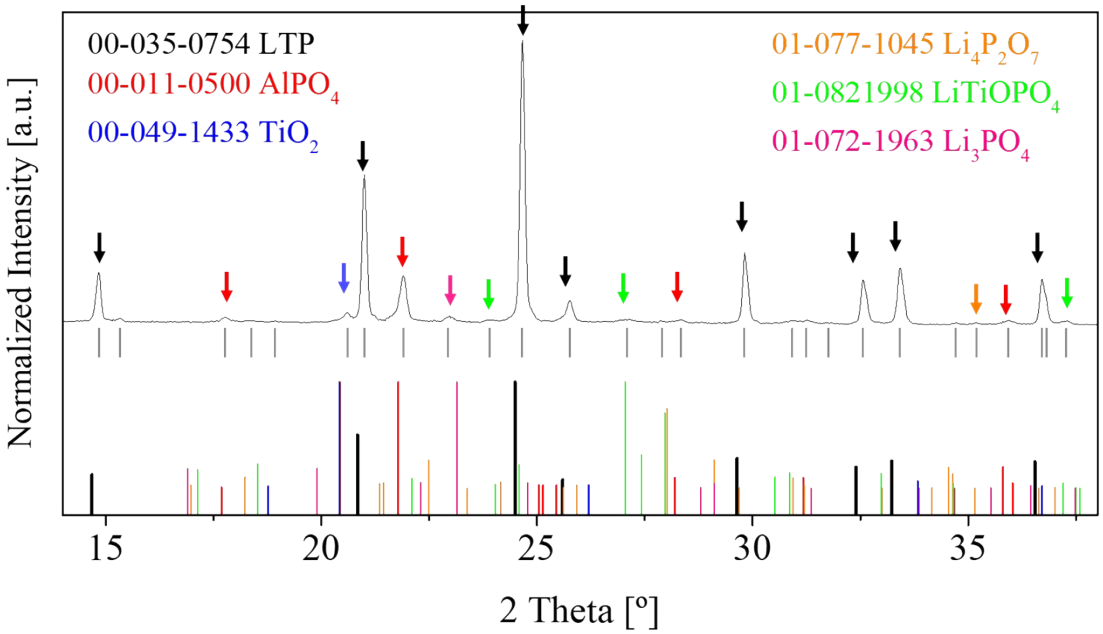

Figure S1. X-ray diffractogram of target before laser ablation presented in linear intensity scale. Corresponding JCPDS files are depicted in the graph. Tentative assignment of the observed main peaks is color-coded accordingly.

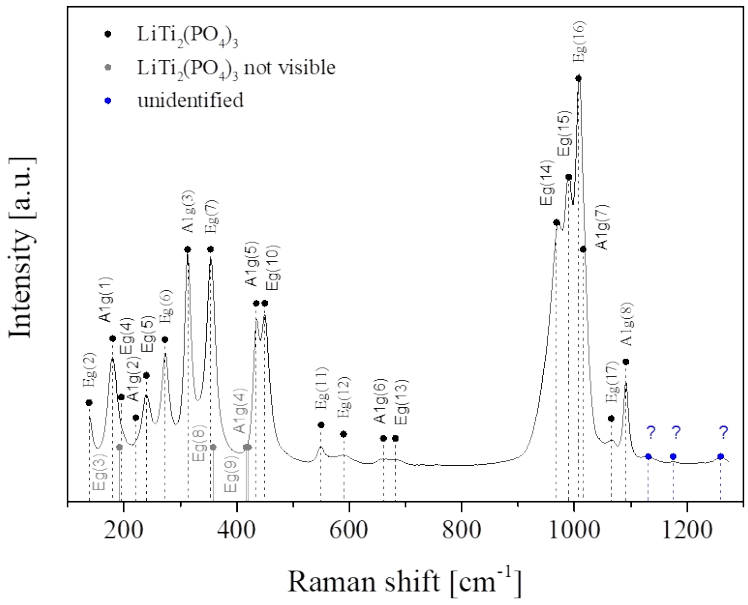

Figure S2. Raman spectrum of the sintered target. Black and grey labels indicate the expected vibrational modes calculated, in which black labels appear in the visible

spectrum and grey modes do not appear.[7] Blue marks could not be assigned to any vibrational mode and remain as unidentified.

Thin films

Thin films are deposited on Silicon chips (100) of 1x1 cm and an additional SiO_2 layer of 100 nm. Either an amorphous Si_3N_4 layer of 300 nm is deposited on top or an additional 10 nm thin Ti adhesive layer for the conductive, poly-crystalline Pt-layer of 80 nm thickness as possible backside contact. For the analysis in NMR, thin films were deposited also on glassy SiO_2 substrates. In a preliminary evaluation of the layer composition, different partial oxygen pressures between 20 – 200 mTorr pO_2 were applied and evaluated by means of EDX, revealing the composition to be the most stoichiometric for layers deposited at 80 mTorr on Si_3N_4 (see Fig. S3).

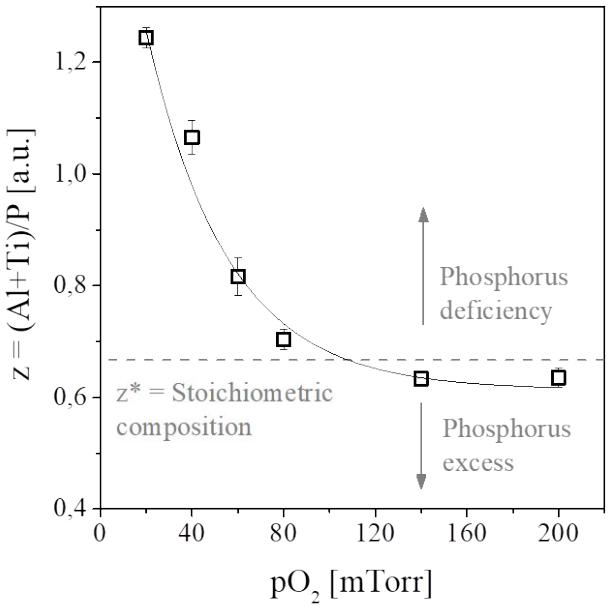

Figure S3. Dependence on the partial oxygen pressure pO_2. EDX results in (a) depict the cation ratio z as function of pO_2 with the optimum stoichiometric composition z* for $z = 2/3$.

Annealing slightly improves the surface roughness of the thin films, as shown in Fig. S4 for AFM images conducted from LATP thin layers deposited on Si_3N_4 substrates

before and after annealing at 800 ºC for 5 h. The reason to separate the deposition and the annealing step is to achieve a low pressure during film growth, that maximizes the Li content and stoichiometry on the film, and a high pressure during annealing, which minimizes Li-losses during film rearrangement. The root mean squared surface roughness Rq are 30±5 nm and 26±6 nm for the as-deposited and the annealed films, respectively.

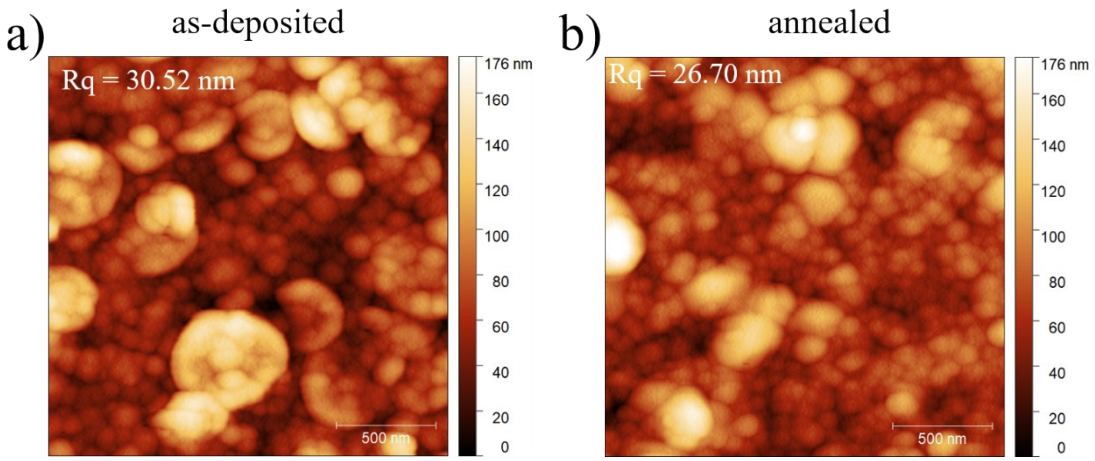

Figure S4. AFM images of the as-deposited (a) and annealed (b) films on Si_3N_4.

The LATP layers reveal a difference in the evolution of crystallinity and crystalline secondary phases in different substrates, such as Fig. S5 proves for the comparison between amorphous Si_3N_4 and SiO_2, to poly-crystalline platinum by Raman spectroscopy and XRD. Whereas Raman spectra do not show any additional phases, the evolution of crystalline TiO_2 and $AlPO_4$ is enhanced on the crystalline Pt substrate, as X-ray diffractograms clearly show. For glassy SiO_2 substrates the conduction of Raman spectra appeared difficult and is therefore neglected in the present work.

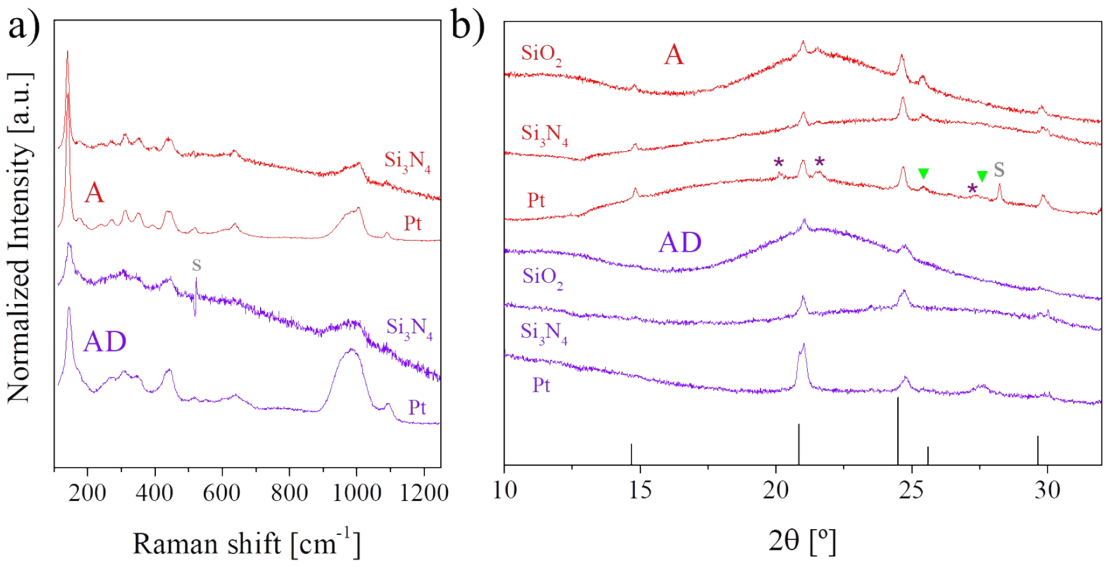

Figure S5. Raman in (a) and XRD measurements in (b) before (AD) and after (A) annealing at 800 °C of samples deposited on either Si_3N_4, SiO_2 glass or Pt. Black vertical lines refer to the undoped $LiTi_2(PO_4)_3$ phase in JCPDS 00-035-0754. Secondary phases are assigned to $AlPO_4$ (violet*, JCPDS 00-046-0551), TiO_2 Anatase (green triangles, JCPDS 01-083-2243 and 01-076-0649) and the substrate (grey s).

Different temperature treatments and dwelling periods for thin films deposited on Si_3N_4 and the evolution of secondary phases is analyzed in Fig. S6a using XRD. The increase in crystalline impurities appears to be the strongest for layers following a slow annealing up to 900 ºC for 1 h (ramp 1º C min^{-1}), whereas treatments at 800 ºC for 5 h or 10 h (ramp 5 ºC min^{-1}) do exhibit only a small difference in secondary phases or crystallinity. To further clarify secondary phases, GI-XRD has been collected in Fig. S6b for thin films as-deposited on Si_3N_4 and annealed at 900 ºC for 1 h (ramp 1 ºC min^{-1}), as well as a LATP thin film annealed on glassy SiO_2 at 800 ºC for 5 h (ramp 5 ºC min^{-1}). Clearly the amount of crystalline secondary phases increases with the annealing and can vary in their composition. Most common secondary phase after annealing is $AlPO_4$ together with different polymorphs and compositions of titania. Further the big

amorphous signal observed from conventional XRD in the theta-2theta arrangement (see Fig. 2a) for AD and A samples is likely related to the amorphous Si_3N_4 substrates as the contribution of the substrate should be minimized when measuring in grazing-incidence. However, some amorphous signal was still observed on films grown on SiO_2, and given the local nature of the amorphous phases present in our films (as shown by NMR and HR-STEM), XRD is not well-suited to reveal this near-order phases.

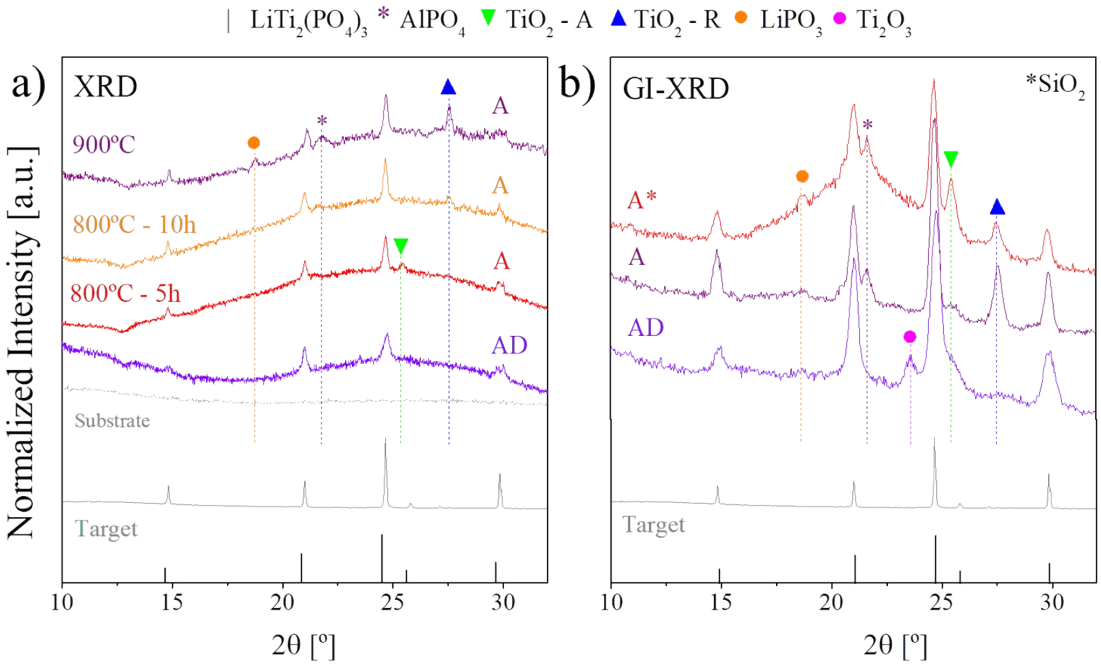

Figure S6. The effect of different annealing temperatures and dwelling time is examined by XRD (a) and GI-XRD (b) for thin films deposited on Si_3N_4 (except for one layer at SiO_2 glass). Black vertical lines refer to the undoped $LiTi_2(PO_4)_3$ phase in JCPDS 00-035-0754. Secondary phases are assigned to $AlPO_4$ (violet*, JCPDS 00-046-0551), TiO_2 Anatase (green triangles, JCPDS 01-083-2243 and 01-076-0649), TiO_2 Rutile (blue triangles, JCPDS 01-087-0710), $LiPO_3$ (orange circle, JCPDS 00-026-1177) and rhombohedral Ti_2O_3 (pink circle, JCPDS 01-076-0145). Violet graphs refer to as-deposited layers, red to a dwelling at 800 ºC (ramp 5 ºC min^{-1}) for 5 h, orange to 800 ºC for 10 h and purple to an annealing at 900 ºC for 1 h and very slow ramping of 1 ºC min^{-1}.

Thin lamellas of the layers, as-deposited (AD) and annealed (A) on Si_3N_4 substrates, were analyzed in the STEM. The FFTs resulting from the HAADF-HRSTEM images for AD and A are shown in Fig. S7. A clear change in the crystalline signal becomes evident when comparing the resulting FFTs of AD images (Fig. S7 (a – c) right) with the FFTs of A samples (Fig. S7 (d – f) right). The clear poly-crystalline diffraction pattern seem to disappear after annealing, leaving ambiguous crystalline signals possibly evolving from single particles, such as visible in Fig. S7e. The formation of an amorphous material acting as intergranular matrix therefore has been proposed, providing a weak amorphous signal in Fig. S7 (d – f), possibly overlaying reflections evolving from the embedded crystalline particles.

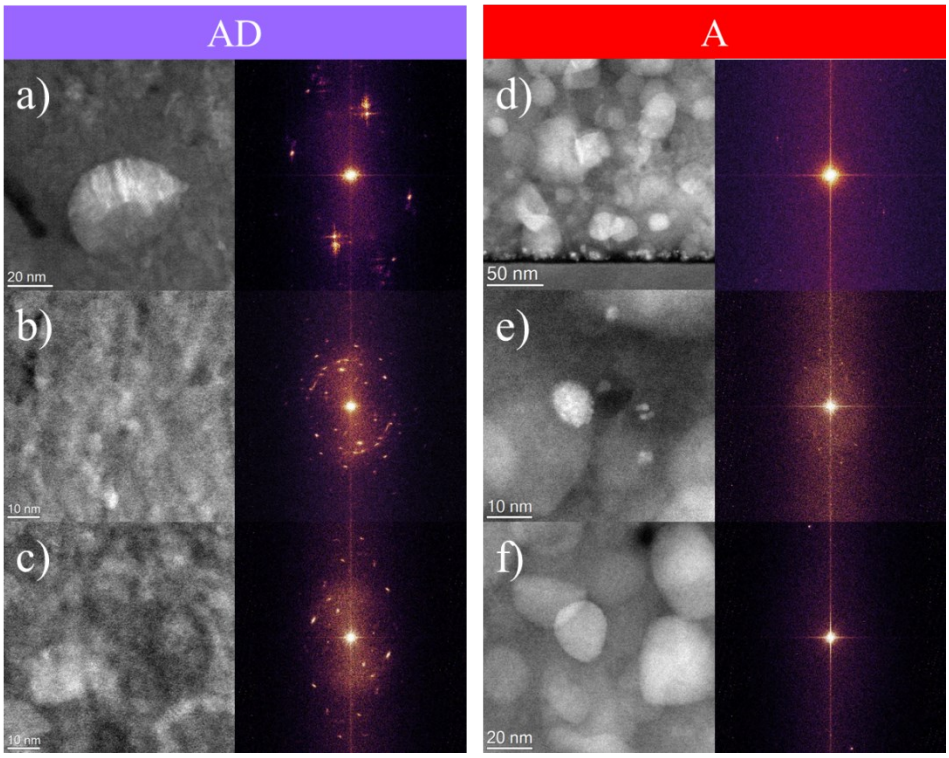

Figure S7. HAADF-HRSTEM images with their corresponding FFTs (full frame) of LATP as-deposited (AD) in (a – c) and annealed (A) at 800 ºC for 5 hrs in (d – f). The left column of each presents the HAADF-HRSTEM image, with the corresponding FFT image to its right.

Impedance measurements were carried out as schematically demonstrated in Fig. S8a and calculated with the parameters d as distance between the electrodes, L as their length and t_f for the film thickness measured in the SEM and spectroscopic ellipsometer.

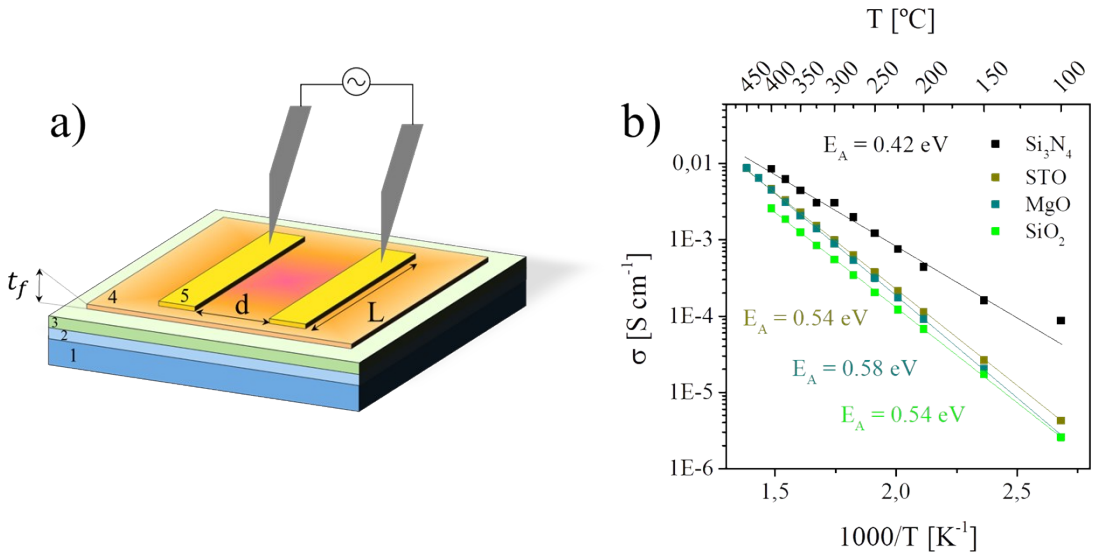

Figure S8. a) In-plane impedance measurement between two electrodes: (1) Silicon chip 1x1cm (100), (2) SiO_2 layer of 100 nm, (3) Si_3N_4 layer of 300 nm, (4) deposited LATP thin film of various thicknesses t_f, (5) sputtered gold electrodes, d as distance between the electrodes and L for the electrode length. b) Arrhenius plot for the as-deposited samples at 80 mTorr on different substrates (Si_3N_4, SiO_2, STO and MgO).

From the measurements performed as shown in Fig. S8a the thin film resistance showed a linear Arrhenius-like behavior, leading to the calculation of the ionic conductivity σ_i of the thin film layer with Eq. S1, where R_{LATP} is the overall resistance of the active solid electrolyte thin film resulting from the first arc in the Nyquist plot ranging from 10 MHz to 1 kHz.

$$\sigma = \frac{1}{R_{LATP}} \cdot \frac{d}{L \cdot t_f} \qquad \text{(Eq. S1)}$$

In the Arrhenius plot shown in Fig. 5b and Fig. S8b it is possible to determine the energy of activation E_A for the overall ionic conductivity in the thin film by using the Arrhenius relation described in Eq. S2 in its exponential shape.

$$\sigma = \sigma_0 \cdot e^{\frac{-E_A}{k_B \cdot T}} \quad \text{(Eq. S2)}$$

Referring to the ionic conductivity σ as rate, σ_0 as pre-exponential factor, k_B as Boltzmann-constant and T as the temperature.

As measurements have been collected in-plane on Si_3N_4 substrates in Fig. 5, the contributions of grain and GBs are not distinguishable due to the presence of a masking high capacitance associated to the SiNx in the Silicon substrate. Taking this into consideration, the first arc in Fig. 5a is related to the overlapped contribution of grain and GB, i.e. $R_{LATP} = R_G + R_{GB}$, in parallel with the previously mentioned SiNx dominant capacity (CPE_{Si}). In series with this ($R_{LATP}CPE_{Si}$) element, there is an additional serial resistance R_s from the electronic contacts. This value appears with a very small contribution, as the impedance measurements were conducted in a pseudo-4-wire measurement setup (see experimental details). The second arc appears with a stronger depression angle of the CPE_{dL} element and further forms a unit with the inclined spike starting at 100 Hz referring to a Warburg element Z_{ct} describing diffusive processes during the charge-transfer (ct). The model for the second arc therefore results in a so-called Randles equivalent circuit, summarizing the electrode-electrolyte or electrolyte-substrate interface ion-blocking processes, which can potentially result in an inter-diffusive lithium intercalation layer.[8–10] In addition to Si_3N_4 substrates, LATP layers were grown on different substrates (STO, MgO and SiO_2) and measured by EIS in-plane. The resulting Arrhenius plot is shown in Fig. S8b, resolving very similar activation energies and ionic conductivities for the as-deposited layers.

Observing different measurements of the same sample deposited on Si_3N_4 in Fig. S9 over a long time range before and after heating up to 450 °C, there was no evidence of degradation due to humidity or temperature in the thin film influencing the ionic conductivity negatively, but anyway the sample appeared to be sensitive. The first arc attributed to the solid electrolyte, its overall ionic conductivity showed inconsistent but negligible changes, whereas the diffusion-controlled processes described by the Randles circuit varied over different heating and cooling cycles. As there is no visible trend evident and variations appear random, a systematical degradation of the material was not observable. But to exclude the possibility of surrounding humidity, all measurements were collected cooling down. There has been reports of instabilities without evident impact on the ionic conductivity, but accelerating degradation in any case, as formerly observed in LATP bulk materials for the stoichiometry especially at grain boundaries.[11]

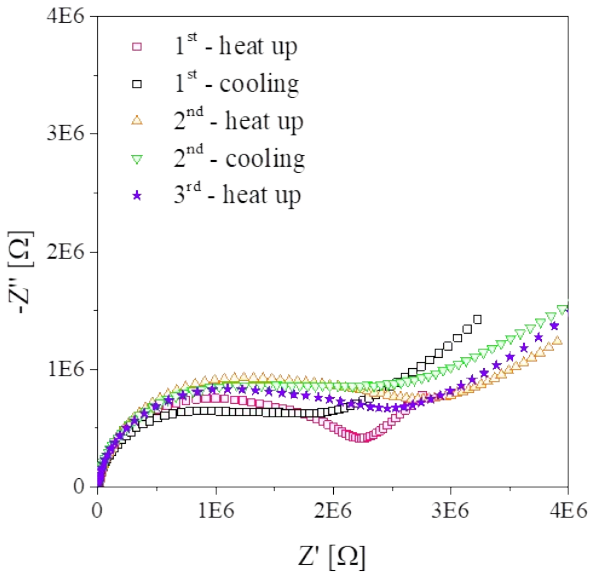

Figure S9. Impedance measurement in air at 200 ºC at the annealed sample deposited at 60 mTorr.

In total the additional heat treatment after annealing leads to higher ionic conductivity, an increase in the pre-exponential factor σ_0 and a lower activation energy

E_A as conducted from the Arrhenius plot for all samples between 20 mTorr to 140 mTorr oxygen partial pressure in Fig. S10. The pO_2 dependence and therefore the influence of stoichiometry are correlated, in which samples deposited at 80 mTorr and 700 ºC improve the most between as-deposited and annealed samples and their ionic conductivities and activation energies.

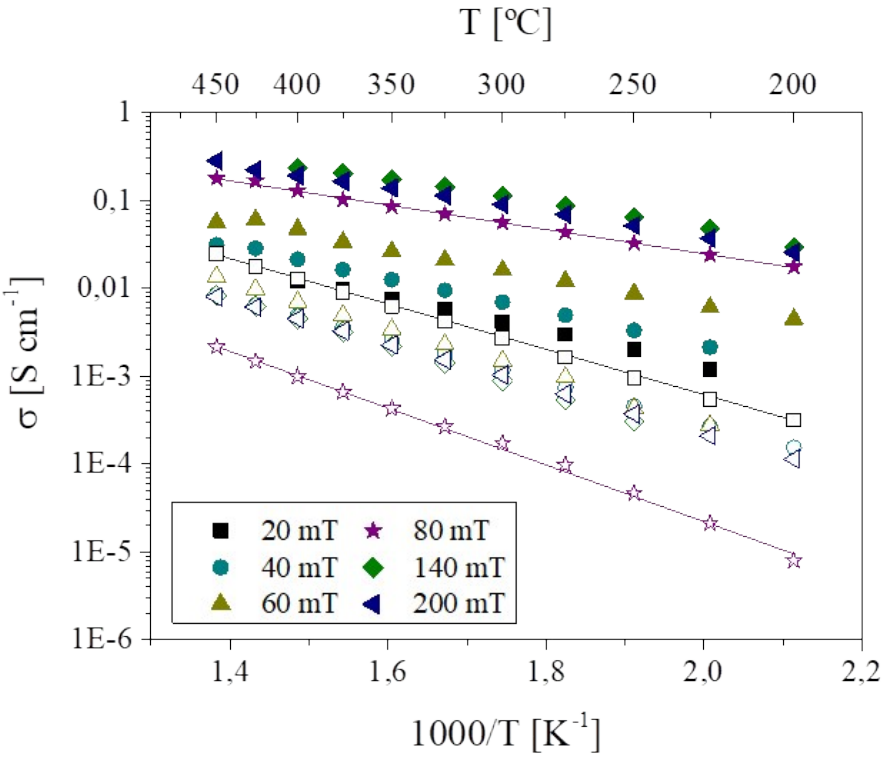

Figure S10. Dependencies for the ionic conductivity on the ^{pO_2} and temperature are plotted as Arrhenius plot in for as-deposited (empty symbols) and annealed (full symbols) samples after an heat treatment at 900 ºC for 1 h (ramp 1 ºC min^{-1}). The deposition at 80 mTorr reveals the highest sensitivity towards annealing, with an increase from 0.71 eV AD to 0.32 eV A.

Different annealing temperatures and dwelling periods have been explored for thin films deposited on Si_3N_4 at 80 mTorr pO_2, as demonstrated in Fig. 6. In order to verify the thin films reproducibility for different as-deposited and annealed layers under comparable conditions, the X-ray diffractograms and Arrhenius plot are shown in Fig. S11. Samples appear to be reproducible, especially as-deposited, supporting the great

stoichiometric control provided in the PLD. Slight differences in the annealed samples can be attributed to minimal variations in the temperature gradients inside the furnace and surrounding conditions, leading to minor variations in the presence of various secondary phases. No significant difference in the electrochemical performance for the layers annealed between 800 – 900 ºC could be deduced from the Arrhenius plot in Fig. S11b. This led to the conclusion to fix the annealing at the minimum temperature with a maximum increase of ionic conductivity at room temperature, which appears to be the annealing at 800 ºC for 5 hrs in air.

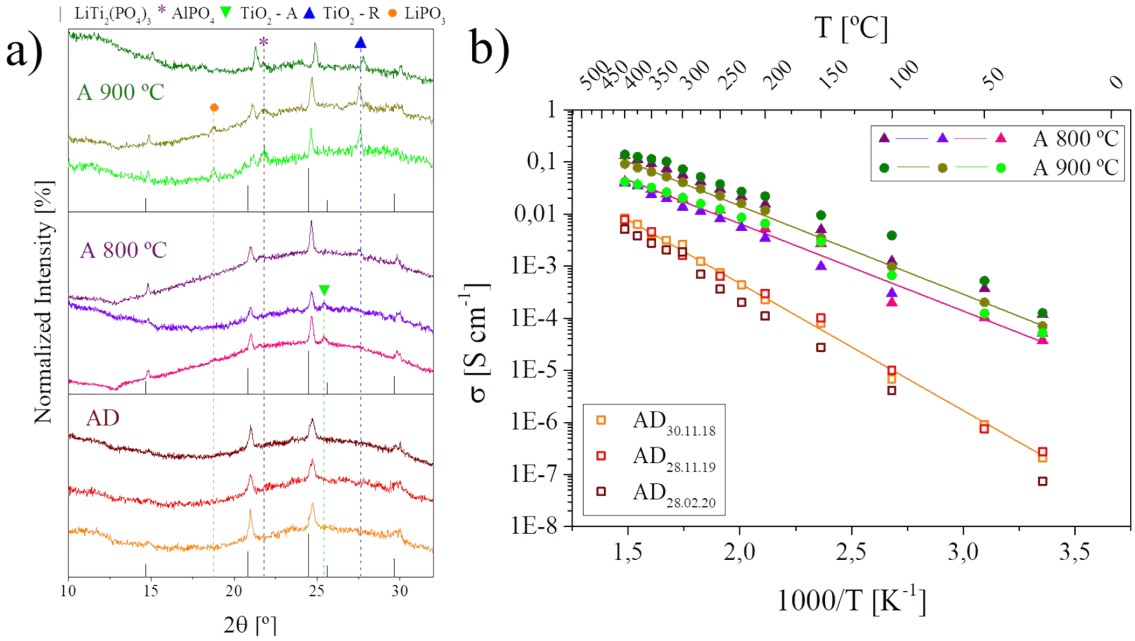

Figure S11. X-ray diffractograms (a) of as-deposited (AD) and annealed (A) samples at different annealing temperatures are shown under reproduced conditions. Subscripts for AD samples indicate their date of deposition by the PLD. In (b) their corresponding ionic conductivities are provided in the Arrhenius plot.

The electrochemical impedance measurements across-plane on LATP thin films as-deposited (AD) and annealed (A) are shown in Fig. S12 for spectra collected at 30 ºC in ambient air. Layers were deposited on Pt-covered Si-substrates and are about 466 nm

in thickness. EIS measurements across-plane were conducted on gold-microelectrodes of 300 µm diameter fabricated on top of the LATP layers.

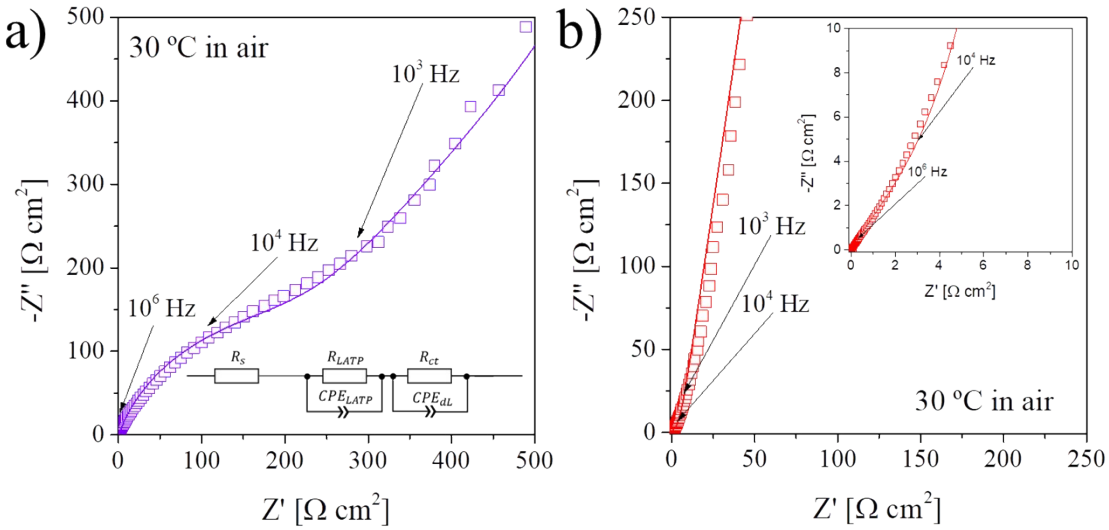

Figure S12. Cross-plane EIS measurements for as-deposited (a) and annealed (b) LATP thin films. Squares indicate the data points collected at different frequencies, lines indicate the corresponding fit with equivalent circuits (see inset in (a)).

To further test battery related electrochemical properties, we carried out measurements of the electrochemical stability window of our LATP films (Figure S13). Measurements were assembled inside an Ar-filled glovebox in an electrochemical cell filled with a liquid electrolyte ($LiPF_6$ EC/DMC), containing Li counter and reference electrodes in a standard three-electrode setup. Cyclic voltammetry was then performed on the LATP films on top of Pt in across-plane configuration. It is clearly seen that the electrochemical stability window of our films is in the range of 2.8-4.5 V, in good agreement with literature values,[12,13] making them compatible with high voltage cathodes.

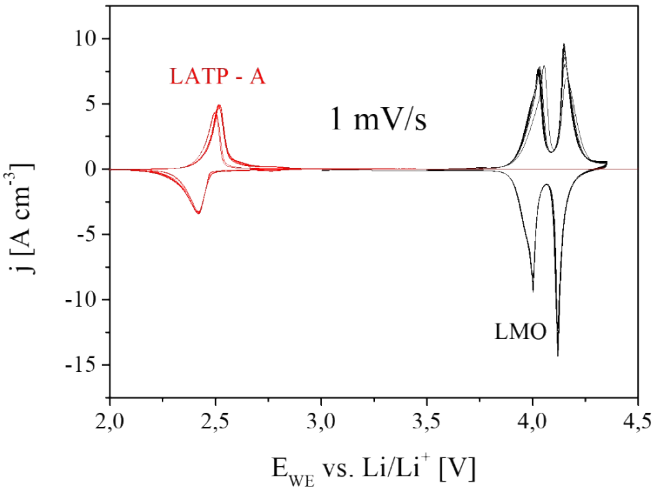

Figure S13. Electrochemical stability window of LATP films by cyclic voltammetry in an organic electrolyte at 1mV/s in across-plane configuration.

We have tracked the thickness of every film that has been grown via Ellipsometry and further confirmed by SEM. In the following graph, we show the thickness for different batches of as-deposited and annealed keeping constant the number of pulses (36000) of the deposition. One can see that there are no significant changes in the thickness between the as-deposited and annealed, especially at the pressure of interest, 80 mTorr.

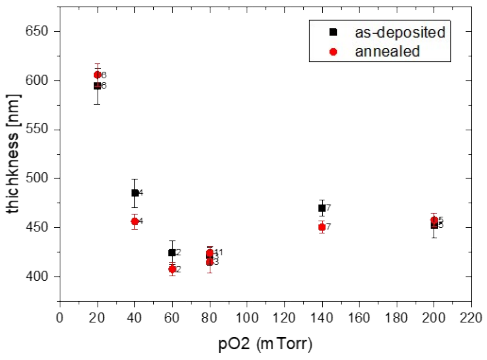

Figure S14. Electrochemical stability window of LATP films by cyclic voltammetry in an organic electrolyte at 1mV/s in across-plane configuration.

References

(1) Aono, H.; Sugimoto, E.; Sadaoka, Y.; Imanaka, N.; Adachi, G. Electrical Properties of Sintered Lithium Titanium Phosphate Ceramics (Li 1+X M X Ti 2−X (PO 4) 3 , M 3+ = Al 3+ , Sc 3+ , or Y 3+). *Chem. Lett.* **1990**, *19* (10), 1825–1828. https://doi.org/10.1246/cl.1990.1825.

(2) Aono, H.; Sugimoto, E.; Sadaoka, Y.; Imanaka, N.; Adachi, G. ya. Electrical Properties and Crystal Structure of Solid Electrolyte Based on Lithium Hafnium Phosphate LiHf2(PO4)3. *Solid State Ionics* **1993**, *62* (3–4), 309–316. https://doi.org/10.1016/0167-2738(93)90387-I.

(3) Arbi, K.; Hoelzel, M.; Kuhn, A.; García-Alvarado, F.; Sanz, J. Structural Factors That Enhance Lithium Mobility in Fast-Ion Li1+x Ti2-x Alx (P O4)3 ($0 \leq x \leq 0.4$) Conductors Investigated by Neutron Diffraction in the Temperature Range 100-500 K. *Inorg. Chem.* **2013**, *52* (16), 9290–9296. https://doi.org/10.1021/ic400577v.

(4) Yu, S.; Mertens, A.; Gao, X.; Gunduz, D. C.; Schierholz, R.; Benning, S.; Hausen, F.; Mertens, J.; Kungl, H.; Tempel, H.; Eichel, R.-A. Influence of Microstructure and AlPO 4 Secondary-Phase on the Ionic Conductivity of Li1.3 Al0.3 Ti1.7 (P O4)3 Solid-State Electrolyte. *Funct. Mater. Lett.* **2016**, *09* (05), 1650066. https://doi.org/10.1142/S1793604716500661.

(5) Key, B.; Schroeder, D. J.; Ingram, B. J.; Vaughey, J. T. Solution-Based Synthesis and Characterization of Lithium-Ion Conducting Phosphate Ceramics for Lithium Metal Batteries. *Chem. Mater.* **2012**, *24* (2), 287–293. https://doi.org/10.1021/cm202773d.

(6) Jiménez, R.; Del Campo, A.; Calzada, M. L.; Sanz, J.; Kobylianska, S. D.; Solopan, S. O.; Belous, A. G. Lithium La0.57 Li0.33 TiO3 Perovskite and Li1.3 Al0.3 Ti1.7 (P O4)3 Li-NASICON Supported Thick Films Electrolytes Prepared by Tape Casting Method. *J. Electrochem. Soc.* **2016**, *163* (8), A1653--A1659.

(7) Giarola, M.; Sanson, A.; Tietz, F.; Pristat, S.; Dashjav, E.; Rettenwander, D.; Redhammer, G. J.; Mariotto, G. Structure and Vibrational Dynamics of NASICON-Type

Li Ti2 (P O4)3. *J. Phys. Chem. C* **2017**, *121* (7), 3697–3706.

(8) Mariappan, C. R.; Yada, C.; Rosciano, F.; Roling, B. Correlation between Micro-Structural Properties and Ionic Conductivity of Li1.5 Al0.5 Ge1.5 (P O4)3 Ceramics. *J. Power Sources* **2011**, *196* (15), 6456–6464. https://doi.org/10.1016/j.jpowsour.2011.03.065.

(9) Barsoukov, E.; Macdonald, J. R. *Impedance Spectroscopy-Theory , Experiment , And*, 2nd ed.; John Wiley & Sons: Hoboken, 2005; Vol. 125.

(10) Iriyama, Y.; Yada, C.; Abe, T.; Ogumi, Z.; Kikuchi, K. A New Kind of All-Solid-State Thin-Film-Type Lithium-Ion Battery Developed by Applying a DC High Voltage. *Electrochem. commun.* **2006**, *8* (8), 1287–1291. https://doi.org/10.1016/j.elecom.2006.03.003.

(11) Dashjav, E.; Ma, Q.; Xu, Q.; Tsai, C. L.; Giarola, M.; Mariotto, G.; Tietz, F. The Influence of Water on the Electrical Conductivity of Aluminum-Substituted Lithium Titanium Phosphates. *Solid State Ionics* **2018**, *321*, 83–90. https://doi.org/10.1016/j.ssi.2018.04.010.

(12) Zheng, F.; Kotobuki, M.; Song, S.; Lai, M. O.; Lu, L. Review on Solid Electrolytes for All-Solid-State Lithium-Ion Batteries. *J. Power Sources* **2018**, *389* (February), 198–213. https://doi.org/10.1016/j.jpowsour.2018.04.022.

(13) Richards, W. D.; Miara, L. J.; Wang, Y.; Kim, J. C.; Ceder, G. Interface Stability in Solid-State Batteries. *Chem. Mater.* **2016**, *28* (1), 266–273. https://doi.org/10.1021/acs.chemmater.5b04082.